DEM - SPH study

~~Study of mixing behaviour~~ of ~~spherical~~ particles in fluid ~~using stirrer~~

dispersion

Dinesh Adepu[1,*], Chuan Yu Wu[1]

[a]*xxx*

Abstract

Keywords: particle dispersion, particle mixing, SPH-DEM, stirrer

1. Introduction

In many,

Particle dispersion is a fundamental physical phenomenon encountered in various industries where powder and fluid interactions are pivotal. Petroleum industry [1], The transport of bodies in internal systems [2], debris flow [3], the food processing industry [4], and ice-sea modeling [5] are a few areas to mention. ~~Particularly,~~ processes ~~involving~~ the mixing of powder with fluid using a stirrer are commonplace [6]. While experimental investigation of such processes is often impractical due to their highly nonlinear nature, numerical methods offer a viable alternative. These systems are studied as part of two-way coupling models. The two-way coupling phenomena are nonlinear, and an analytical study is not feasible. A numerical study is preferable while handling such a phenomenon. A mesh-based or meshless technique can be utilized to study rigid fluid coupling (RFC) numerically. Figure 2 illustrates a sample particle dispersion problem studied in the current work.

The combination of Discrete Element Method (DEM) for solid particle interactions and Computational Fluid Dynamics (CFD) for fluid modeling is a classic approach in handling particulate flow problem. In mesh-based CFD-DEM modeling, lattice Boltzmann method (LBM) [7] and finite volume method (FVM) [8] are utilized to handle the fluid dynamics. Similarly, in meshless schemes like Smoothed Particle Hydrodynamics (SPH) [9], Moving

this part is not very logical, the connections/transitions between sentences/statements look random. suggest to re-write!

*Corresponding author

Email addresses: d.dinesh@surrey.ac.uk (Dinesh Adepu), XXX (Chuan Yu Wu)

beware of CFD, LBM being different methods, FVM may be a subset of CFD

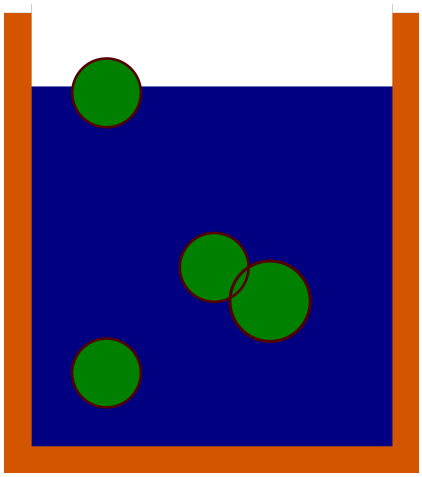

Figure 1: An illustrative figure showcasing the dispersion of particles within a free surface tank.

Particle Semi-implicit (MPS), and Particle Finite Element Method (PFEM) [10, 11], handles the fluid dynamics. While handling the interaction between the fluid and solid particles, the interaction can be categorized into a resolved and unresolved coupling. In unresolved coupling, simplified models compute forces acting on solid particles within fluid flow, while fully resolved coupling computes forces comprehensively. Both strategies are applicable in both meshless [12, 13] and mesh-based [14, 15] CFD-DEM techniques. Research such as [16] and [9] explore wide particle size distributions with CFD-DEM and SPH-DEM respectively. Regarding non-Newtonian fluid modeling in mesh-based schemes, works like [17] are notable and in meshless schemes, [9] is notable. Zhu et al. [18] and Ma et al. [15] delve into investigations on spherical and non-spherical particles respectively within CFD-DEM frameworks. Meshless CFD-DEM, though fruitful, encounters challenges in handling problems with free surfaces and becomes computationally demanding with a large number of solid particles, especially in fully resolved coupling. In contrast, SPH offers advantages in such scenarios due to its inherent capability in handling free surfaces and adeptness in modeling large mesh deformation problems, facilitating the incorporation of novel physics.

The SPH method is a meshless numerical method originally proposed by Gingold and Monaghan [19] and Lucy [20] to model astrophysics problems. It has been extensively applied to simulate problems involving fluids, structural dynamics, fluid-structure interaction, granular physics, non-Newtonian fluid

flows [9] among other areas [21]. Various kind of particulate flows, involving, simple spherical particles mixing using unresolved coupling [12, 22] and ~~with~~ debris flow [23] with fully resolved coupling approach ~~has been solved~~ using SPH-DEM ~~framework~~. Handling particles of arbitrary shape in fluid flow is addressed in various works, including those by Peng et al. [9], Canelas et al. [23], Amicarelli et al. [24]. Several variants of SPH, such as WCSPH [9**?**], and ISPH [25], are utilized for modeling fluid flow with particulate flows. The coupling between fluid and rigid bodies in the fully resolved category employs techniques such as the fixed ghost particle technique [23, 25], single layers of dummy SPH particles [9], and simple repulsive forces [26]. Coupling between SPH fluid particles and solid structures discretized as vertex edges is proposed by [27]. Particle settling with variable sizes is studied by Zou et al. [28]. Elastic behavior of spherical particles and dispersion studies are conducted by Ng et al. [29]. Interaction between rigid bodies of arbitrary sizes is addressed using various techniques, such as those discussed in papers by Asai et al. [25], citetpeng2021fully, Canelas et al. [23].

In the current work we cosider ~~the~~ particle dispersion within a large-scale under stirrer mixing phenomenon. We employ Smoothed Particle Hydrodynamics (SPH) to model fluid dynamics and the Discrete Element Method (DEM) to handle the dynamics and contact interactions among spherical particles. The interaction between solids and fluids is ~~managed~~ using a fixed ghost particle approach, ensuring a fully resolved simulation. We validate the fluid solver independently using Poiseuille flow and the DEM solver separately using fundamental benchmarks such as particle-particle and particle-wall impacts. Subsequently, the fully resolved coupled SPH-DEM solver is validated using three benchmarks: a single particle entering, two particles settling, and a forced wedge entry into a steady hydrostatic tank. Upon confirming the fidelity of the solver, we proceed with analyzing the mixing behavior of various spherical particles influenced by a stirrer in a ~~water~~ tank. We investigate scenarios involving particles of different densities, stirrer velocities, and variable sizes as part of our case study. The development work is conducted using PySPH[30], an open-source code available at `https://github.com/pypr/pysph` . To ensure reproducibility, we utilize the automan package [31] to automate all results generated in the current manuscript, aiming for a reproducible research approach.

The structure of this paper is as follows: In section 2, we explain the numerical method used to model fluid dynamics. Section 3 outlines the equations governing the dynamics of rigid bodies and the contact force model em-

ployed to resolve collisions among them. The coupling between rigid spherical particles and the fluid is detailed in section 4. Our results are presented in section 6, where various problems from the literature are simulated to validate the current solver, and particle dispersion is examined.

2. Fluid modeling

In the current work, we follow a weakly-compressible SPH approach to model the fluid. Smoothed particle hydrodynamics is initially developed by Lucy [20] and Gingold and Monaghan [19] to model astrophysical problems. The continuum in SPH is modeled using particles, which has physical properties such as mass, velocity, and the particles interact based on the governing equations using a Guassian-like kernel [?].

2.1. Fluid governing equations

Equations governing the fluid motion are, conservation of mass

$$\frac{d\rho}{dt} = -\rho \frac{\partial u_i}{\partial x_i}, \tag{1}$$

and conservation of linear momentum,

$$\frac{du_i}{dt} = \frac{1}{\rho} \frac{\partial \sigma_{ij}}{\partial x_j} + g_i, \tag{2}$$

where ρ is the density, u_i is the i^{th} component of the velocity field, x_j is the j^{th} component of the position vector, g_i is the component of body force per unit mass and σ_{ij} is stress tensor.

The stress tensor is split into a pressure and viscous parts,

$$\sigma_{ij} = -p\delta_{ij} + 2\eta \frac{\partial u_i}{\partial x_j} \tag{3}$$

where η is the kinematic viscosity of the fluid, p is the pressure, δ_{ij} is the Kronecker delta function.

2.2. Discretized fluid governing equations

The governing equations involve function, derivative and divergence operators. In SPH, these operators are approximated based on the positions, mass and the kernel values of the discretized particles. Assume that the

domain is discretized into N particles with mass m_i and volume Δv_i, We have

$$m_j = \Delta v_i \, \rho_i. \tag{4}$$

Based on this discretization, the discrete function approximation is given as,

$$A_i = \sum_{j \in \text{Neigh}(i)} \frac{m_j}{\rho_j} A_j \, W(\mathbf{x}_i - \mathbf{x}_j, h), \tag{5}$$

where $A(\boldsymbol{x}_i) = A_i$ is the value of the field property of particle i, similarly for A_j. Here, Neigh(i) is the neighbours of particle i. A symmetric derivative approximation [32] is given as,

$$\nabla A(\mathbf{x}_i) = \rho_i \sum_j m_j \left(\frac{A_i}{\rho_i^2} + \frac{A_j}{\rho_j^2} \right) \nabla W_{ij}. \tag{6}$$

A symmetric gradient operator ensures equal and opposite forces acting on the particles.

An approximation of the divergence operator is used to discretize the eq. (1). It is given as,

$$\nabla \cdot \mathbf{v}(\mathbf{x}_i) = \frac{1}{\rho_i} \sum_j m_j \, (\mathbf{v}_j - \mathbf{v}_i) \cdot \nabla W_{ij}. \tag{7}$$

The SPH discretization of the continuity equation eq. (8) and the momentum equation eq. (9) respectively are,

$$\frac{d\rho_a}{dt} = \sum_b \frac{m_b}{\rho_b} \, \rho_a \, \mathbf{u}_{ab} \cdot \nabla_a W_{ab}, \tag{8}$$

Similarly, the discretized momentum equation for fluids is written as,

$$\frac{d\mathbf{u}_a}{dt} = -\sum_b m_b \left(\frac{p_a}{\rho_a^2} + \frac{p_b}{\rho_b^2} \right) \nabla_a W_{ab} + \sum_b m_b \frac{4\eta \nabla W_{ab} \cdot \mathbf{r}_{ab}}{(\rho_a + \rho_b)(r_{ab}^2 + 0.01 h_{ab}^2)} \mathbf{u}_{ab} + \mathbf{g}_a, \tag{9}$$

where $\mathbf{I}$ is the identity matrix, η is the kinematic viscosity of the fluid and [33] formulation is used to discretize the viscosity term.

We add to the momentum equation an additional artificial viscosity term Π_{ab} [34] to maintain the stability of the numerical scheme, given as,

$$\Pi_{ab} = \begin{cases} \frac{-\alpha h_{ab} \bar{c}_{ab} \phi_{ab}}{\bar{\rho}_{ab}} & \mathbf{u}_{ab} \cdot \mathbf{r}_{ab} < 0, \\ 0 & \mathbf{u}_{ab} \cdot \mathbf{r}_{ab} \geq 0, \end{cases} \tag{10}$$

where,

$$\phi_{ab} = \frac{\mathbf{u}_{ab} \cdot \mathbf{r}_{ab}}{r_{ab}^2 + 0.01 h_{ab}^2}, \tag{11}$$

where $\mathbf{r}_{ab} = \mathbf{r}_a - \mathbf{r}_b$, $\mathbf{u}_{ab} = \mathbf{u}_a - \mathbf{u}_b$, $h_{ab} = (h_a + h_b)/2$, $\bar{\rho}_{ab} = (\rho_a + \rho_b)/2$, $\bar{c}_{ab} = (c_a + c_b)/2$, and α is the artificial viscosity parameter. The pressure p_a is evaluated using an equation of state:

$$p_a = K \left(\frac{\rho_a}{\rho_0} - 1 \right). \tag{12}$$

Where, $K = \rho_0 c_0^2$ is bulk modulus of the body, with $c_0 = 10 \times V_{\max}$ is speed of sound, while ρ_0 as the initial density of the particles.

2.3. Boundary Conditions

The ghost particle approach of [35] is used to model the boundaries. We use three layers of ghost particles to model the solid wall. The properties of the solid wall are interpolated from the fluid particles.

When the viscous force is computed, the no slip boundary condition is used, where the velocity on the boundary set as,

$$\mathbf{u}_{\mathrm{Ga}} = 2\mathbf{u}_{\mathrm{p}} - \hat{\mathbf{u}}_{\mathrm{a}}. \tag{13}$$

The projected velocity $\hat{\mathbf{u}}_{\mathrm{a}}$ on the ghost particles is computed using,

$$\hat{\mathbf{u}}_a = \frac{\sum_b \mathbf{u}_b W_{ab}}{\sum_b W_{ab}}, \tag{14}$$

where $\mathbf{u}_b$ is the momentum velocity of the fluid and W_{ab} is the kernel value between the fluid particle and the ghost particle.

The pressure of the boundary particle is extrapolated from its surrounding fluid particles by the following equation,

$$p_w = \frac{\Sigma_f p_f W_{wf} + (\mathbf{g} - \mathbf{a_w}) \cdot \Sigma_f \rho_f \mathbf{r}_{wf} W_{wf}}{\Sigma_f W_{wf}}, \tag{15}$$

where $\mathbf{a}_w$ is the acceleration of the wall. The subscript f denotes the fluid particles and w denotes the wall particles.

3. Rigid body dynamics

As we only consider spheres or simple shapes, much of the discussions in this section can be simplified

not proper sentence

The equations governing the dynamics of a rigid body are, balance of linear and angular momentum given by,

$$\frac{d\left(M\mathbf{v}_{cm}\right)}{dt} = \sum_i \mathbf{F}_i, \tag{16}$$

$$\frac{d\mathbf{L}}{dt} = \boldsymbol{\tau}_{cm}, \tag{17}$$

where M, $\mathbf{v}_{cm}$ are the mass and velocity of the center of mass of the rigid body. $\mathbf{F}_i, \boldsymbol{\tau}_{cm}, \mathbf{L}$ are force acting at point i, torque and angular momentum about the center of mass of the rigid body. In the current case, force acting on the particle i, $\mathbf{F}_i$, is due to the interaction with the other bodies and with the fluid particles, and any other body forces. The torque $\boldsymbol{\tau}_{cm}$ and angular momentum $\mathbf{L}$ are computed as,

$$\boldsymbol{\tau}_{cm} = \sum_i \mathbf{F}_i \times (\mathbf{x}_{cm} - \mathbf{x}_i), \tag{18}$$

$$\boldsymbol{L} = \sum_i \mathbf{r}_i \times \ (\boldsymbol{\omega} \times \mathbf{r}_i) = \sum_i m_i \left[(\mathbf{r}_i \cdot \mathbf{r}_i)\mathbf{I} - \mathbf{r}_i \otimes \mathbf{r}_i\right]. \tag{19}$$

Here $\mathbf{x}_{cm}$ and ω are the position of the center of mass and angular velocity of the rigid body. m_i, $\mathbf{x}_i$, $\mathbf{r}_i$ are the mass, position of particle, and position of particle i with respect to vector center of mass.

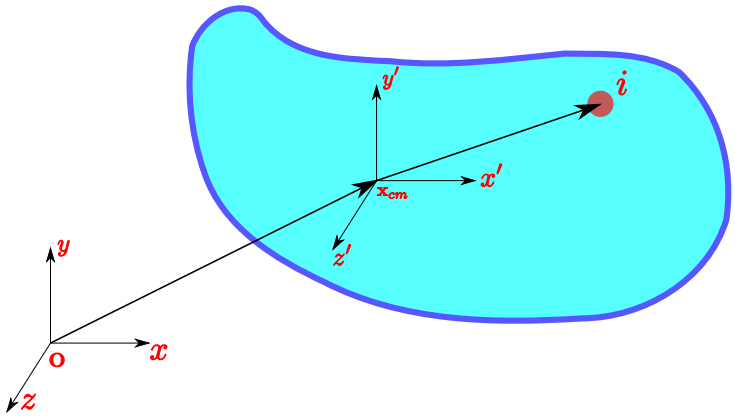

Figure 2: Body frame and local frame description of rigid body

Global ?

global and local frames ?

We use two coordinate frames to capture the dynamics of the rigid body, a global frame and a body frame as shown in fig. 2. The body fixed frame, which moves with rigid body is always located at the center of mass ($\mathbf{x}_{cm}$). The state of the rigid body at a given time (t) can be described using position ($\mathbf{x}_{cm}$) and velocity ($\mathbf{v}_{cm}$) of the center of mass, a rotation matrix($\mathbf{R}$) to represent the orientation of the rigid body with respect to the global frame, and angular velocity($\boldsymbol{\omega}$). The center of mass is computed as

$$\mathbf{x}_{cm} = \frac{\sum_i m_i \, \mathbf{x}_i}{\sum_i m_i}. \tag{20}$$

What are m_i, x_i, ?

The position of the discretized particle (i) in fig. 2 belonging to the rigid body at time t can be computed as,

$$\mathbf{x}_i = \mathbf{x}_{cm} + \mathbf{r}_i, \tag{21}$$

with

$$\mathbf{r}_i = \mathbf{R}\bar{\mathbf{r}}_i. \tag{22}$$

Here $\bar{\mathbf{r}}_i$ is the position of the particle i about the body frame axis and remains constant through out the simulation. The rotation matrix $\mathbf{R}$ is used to bring the body frame position vector to the global frame $\mathbf{O}$. Similarly the velocity vector is computed as,

$$\mathbf{v}_i = \mathbf{v}_{cm} + \boldsymbol{\omega} \times \mathbf{r}_i. \tag{23}$$

We evolve the state of the rigid body through the integration of the eqs. (16) and (17). The linear velocity of the center of mass ($\mathbf{v}_{cm}$) and angular momentum ($\mathbf{L}$) at the next timestep are computed as,

$$\mathbf{v}_{cm}^{n+1} = \mathbf{v}_{cm}^{n} + \frac{\mathbf{F}_{cm}}{M} \, \Delta t, \tag{24}$$

$$\mathbf{L}^{n+1} = \mathbf{L}^{n} + \boldsymbol{\tau}_{cm} \, \Delta t. \tag{25}$$

Here, $\mathbf{F}_{cm} = \sum_i \mathbf{F}_i$.

The position of the center of mass and the rotation matrix ($\mathbf{R}$) are updated by,

$$\mathbf{x}_{cm}^{n+1} = \mathbf{x}_{cm}^{n} + \mathbf{v}_{cm}^{n} \, \Delta t, \mathbf{R}^{n+1} = \mathbf{R}^{n} + \tilde{\boldsymbol{\omega}}^{n} \, \mathbf{R}^{n} \, \Delta t, \tag{26}$$

where $\tilde{\boldsymbol{\omega}}^n$ is matrix formulation of angular velocity ω. The angular velocity at the new time step is computed with

$$\boldsymbol{\omega}^{n+1} = (\boldsymbol{I}^{-1})^{n+1} \, \mathbf{L}^{n+1}. \tag{27}$$

Here, moment of inertia at the new time step is computed as,

$$(\boldsymbol{I}^{-1})^{n+1} = \mathbf{R}^{n+1}\overline{\boldsymbol{I}}^{-1}(\mathbf{R}^{n+1})^T. \tag{28}$$

where moment of inertia ($\overline{\boldsymbol{I}}^{-1}$) in body frame is used to compute in global frame at every time instant for faster computations. The moment of inertia ($\overline{\boldsymbol{I}}$) is computed as,

$$\overline{\boldsymbol{I}} = \begin{bmatrix} \sum_i m_i(y_i^2+z_i^2) & -\sum_i m_i x_i y_i & -\sum_i m_i x_i z_i \\ -\sum_i m_i x_i y_i & \sum_i m_i(x_i^2+z_i^2) & -\sum_i m_i y_i z_i \\ -\sum_i m_i x_i z_i & -\sum_i m_i y_i z_i & \sum_i m_i(x_i^2+y_i^2) \end{bmatrix}.$$

The position and velocity of the particles of the rigid body are updated by

$$\mathbf{r}_i = \mathbf{R}\cdot\bar{\mathbf{r}}_i, \tag{29}$$

$$\mathbf{x}_i = \mathbf{x}_{cm} + \mathbf{r}_i, \tag{30}$$

$$\mathbf{v}_i = \mathbf{v}_{cm} + \boldsymbol{\omega}\times\mathbf{r}_i. \tag{31}$$

The force acting on particle i is composed of interaction with the other rigid bodies, and the fluid, given as

$$\mathbf{F}_i = \mathbf{F}^i_{\text{Fl}} + \mathbf{F}^i_{\text{cont}} \tag{32}$$

We follow section 3.1 to compute force $\mathbf{F}^a_{\text{cont}}$ acting on particle i due to the interaction with the rigid bodies. The force $\mathbf{F}^i_{\text{rfc}}$ acting due to the interaction with the fluid particles follows section 4.

3.1. Contact ~~resolution~~ models

We resolve the contact among the spherical particles using discrete element method. In the current work we have utilized a non-linear contact force model. In DEM, the force acting on a particle a due to the interaction with the particle b is resolved into a normal and tangential component. The normal force component is utilised to make sure that the particle do not penetrate into each other, while the tangential component is used to model the friction between the interacting particles. The normal force ($\boldsymbol{F}^n_a$) on particle a due to the interaction with the particles b is given by a non-linear, Hetzian model Brilliantov et al. [36],

$$\mathbf{F}^n_a = k_r\delta_n\mathbf{n}. \tag{33}$$

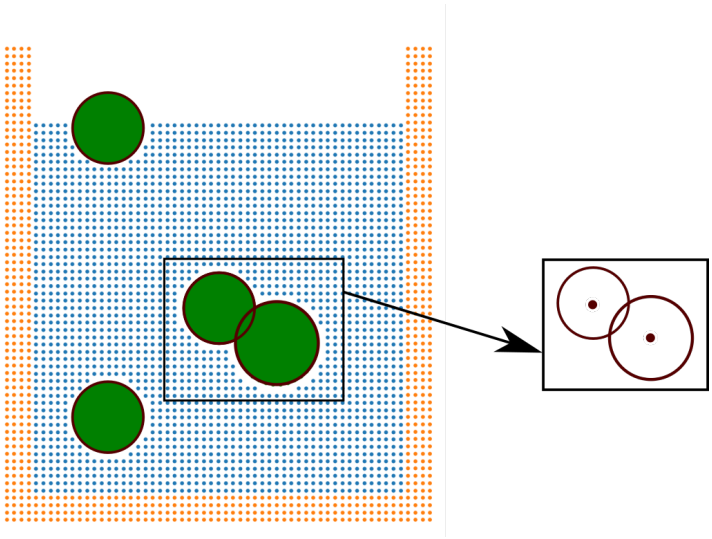

Figure 3: Demonstration of contact handling between two rigid spherical particles immersed in a fluid tank.

Here, the overlap δ_n is computed using

$$\delta_n = R_a + R_b - r_{ab}, \tag{34}$$

k_r is the normal spring stiffness coefficient, which is computed using the material properties of the bodies in contact [37].

3.2. Tangential force computation

To handle the frictional contact, we associate a tangential spring attached to particle a and particle b to compute the tangential force, which initially has a magnitude of zero ($|\Delta \boldsymbol{l}_a| = 0$). The tangential spring is activated when the particle comes into contact with particle b. The tangential force is history-dependent. The contact friction force is proportional to the tangential spring displacement, which is integrated over the contact time as

$$\mathbf{F}_a^{t^{n+1}} = -k_f \Delta \boldsymbol{l}_a^{n+1} = -k_f \left[\left(\Delta \boldsymbol{l}_a^n + \mathbf{v}_{ab}^{n+1} \Delta t \right) \cdot \mathbf{t}_a^{n+1} \right] \mathbf{t}_a^{n+1}, \tag{35}$$

where Δt is the time step, $\mathbf{v}_{ab} = \mathbf{v}_a - \mathbf{v}_b$ is the relative velocity of particle a with respect to the contacting particle b, and k_f is the tangential spring stiffness coefficient. The tangential spring stiffness is computed similar to the normal spring stiffness[37]. The tangential unit vector is computed by,

$$\mathbf{t}_a = \frac{\mathbf{v}_{ab} - (\mathbf{v}_{ab} \cdot \mathbf{n})\mathbf{n}}{|\mathbf{v}_{ab} - (\mathbf{v}_{ab} \cdot \mathbf{n})\mathbf{n}|}. \tag{36}$$

The tangential force is coupled to the normal force through the Coulomb's law,

$$\mathbf{F}_a^t = \min(\mu|\mathbf{F}_a^n|, |\mathbf{F}_a^t|)\ \frac{\mathbf{F}_a^t}{|\mathbf{F}_a^t|}. \tag{37}$$

This allows us to impose the sliding friction condition between the interacting solids. Finally, the total force acting on the particle a due to the interaction with particle b is:

$$\mathbf{F}_a^{\text{cont}} = \mathbf{F}_a^n + \mathbf{F}_a^t \tag{38}$$

An equal and opposite force of the same magnitude is applied to particle b, given as

$$\mathbf{F}_b^{\text{cont}} = -\mathbf{F}_a^{\text{cont}}. \tag{39}$$

4. Rigid fluid coupling

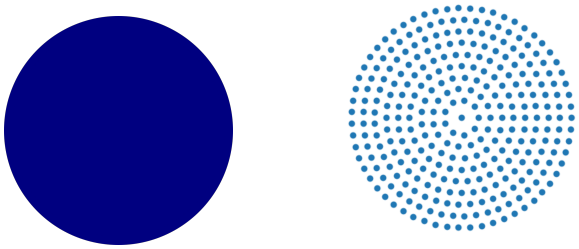

(a) A rigid spherical particle

(b) A rigid spherical particle sampled with dummy SPH particles

Figure 4 add caption here .

To calculate the force exerted on the spherical particle by the surrounding fluid, we employ a method involving the sampling of the spherical particle using dummy Smoothed Particle Hydrodynamics (SPH) particles, depicted in fig. 4. These SPH particles are evenly distributed and remain stationary, moving in tandem with the velocity of the rigid particle at any given location. To establish the pressure of these SPH particles, we utilize the fixed ghost particle boundary technique outlined in section 2.3.

With spherical particles being discretized into SPH particles and immersed in fluid can be seen in fig. 5. The force on the fluid particle due to the interaction with the sampled dummy SPH particles is considered in the momentum eq. (9) and the continuity eq. (8). The force acting on the

did you use 3 layers of Ghost particles, or the whole body?

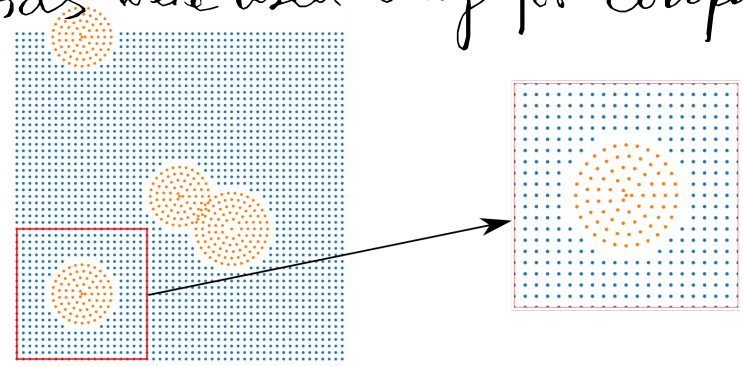

Figure 5: A rigid spherical particle sampled with dummy SPH particles being immersed in a fluid tank. An SPH particle representation

sampled dummy SPH particle due to the interaction with the fluid is given by,

$$\mathbf{F}^a_{\text{rfc}} = -m_a \sum_f m_f \left(\frac{p_f}{\rho_f^2} + \frac{p_a}{\rho_a^2} \right) \nabla_a W(x_{af}). \tag{40}$$

Here, m_a signifies the hydrodynamic mass of the sampled dummy SPH particle, and ρ_a represents its hydrodynamic density. While m_f, p_f and ρ_f are mass, pressure and density of the fluid particle.

5. Time Integration

We use the kick-drift-kick scheme for the time integration. We move the velocities of the fluid and the solid particles to half time step,

$$\mathbf{u}_a^{n+\frac{1}{2}} = \mathbf{u}_a^n + \frac{\Delta t}{2} \left(\frac{d\mathbf{u}_a}{dt} \right)^n, \tag{41}$$

Then the time derivative of density is calculated using the eq. (8) using the velocities at half time step. The new time step density and particle position is updated by,

$$\rho_a^{n+1} = \rho_a^n + \Delta t \left(\frac{d\rho_a}{dt} \right)^{n+\frac{1}{2}}, \tag{42}$$

$$\mathbf{r}_a^{n+1} = \mathbf{r}_a^n + \Delta t \, \mathbf{u}_a^{n+1}. \tag{43}$$

Finally, at new time-step particle position, the momentum velocity is updated

$$\mathbf{u}_a^{n+1} = \mathbf{u}_a^{n+\frac{1}{2}} + \frac{\Delta t}{2} \left(\frac{d\mathbf{u}_a}{dt} \right)^{n+1}. \tag{44}$$

The modeling of rigid-rigid interaction requires ~~lower~~ time step than the fluid. We choose the minimum of ~~both the~~ timesteps to move the system forward in time. For the numerical stability of fluid, the time step depends on the CFL condition as,

$$\Delta t_{\text{fluid}} = \min\left(0.25\,\frac{h}{c+|U|}, 0.25\,\frac{h^2}{\nu}, 0.25\,\frac{h^2}{g}\right), \tag{45}$$

where $|U|$ is the maximum velocity magnitude, c is the speed of sound typically chosen as $10|U|$ for fluids in this work. For rigid body, the time step is constrained as,

$$\Delta t_{\text{rb}} \leq \frac{\pi}{50}\sqrt{\frac{m}{k_r}}. \tag{46}$$

A minimum timestep is chosen as

$$\Delta t = min(\Delta t_{\text{fluid}}, \Delta t_{\text{rb}}). \tag{47}$$

6. Results

Initially, we validate our fluid solver through the resolution of the Poiseuille flow problem. Subsequently, we validate the Discrete Element Method (DEM) solver by simulating a normal head-on collision between two spherical particles and addressing a particle-wall impact scenario. We validate the coupled Smoothed Particle Hydrodynamics (SPH)-DEM solver is confirmed through simulations involving a spherical particle entering a steady tank and a falling solid in a water tank and a floating solid. Lastly, we investigate the mixing behavior of spherical particles under a stirrer, examining cases with varying densities and diameters.

6.1. Poiseuille's flow

We study unsteady flow between two infinite, parallel paltes at rest in presence of pressure gradient to validate our fluid solver implementation. The plates are placed 1 m apart vertically, where the fluid is driven due to a pressure gradient, a form of body force. The flow is towards positive x direction. The schematic is shown in fig. 6. In this exact conditions, the Navier-Stokes equations admit the time dependent solution given in eq. (48), as given by Morris et al. [33]

$$v_x(y,t) = \frac{F}{2\nu}y(y-L) + \sum_{n=0}^{\infty}\frac{4FL^2}{\nu\pi^3(2n+1)^3}\sin\left(\frac{\pi y}{L}(2n+1)\right)\exp\left(\frac{(2n+1)^2\pi^2\nu}{L^2}t\right) \tag{48}$$

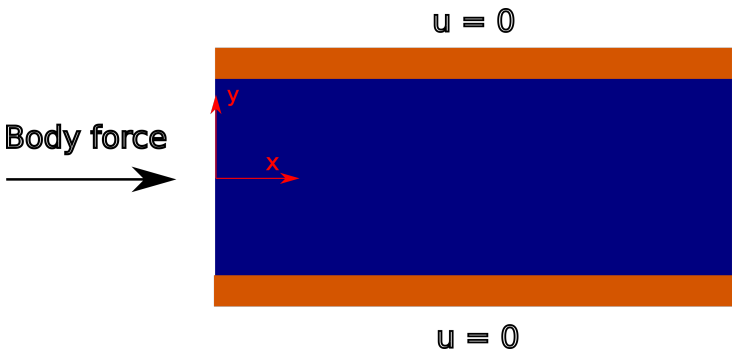

Figure 6: Poiseuille flow problem: Schematic of a fluid being driven in between two parlell plates due to a pressure gradient force.

ν is kinematic viscosity ($\frac{\mu}{\rho_0}$). This test case serves to validate the no-slip boundary condition of our developed scheme. We use numerical parameters such as a viscosity of 0.01, a particle spacing of $\frac{1}{60}$, and set the speed of sound to ten times the maximum velocity the fluid can attain. The simulation runs for a total duration of 50 seconds.

Figure 7 depicts the variation of the u-velocity in y-direction, compared to the analytical formula given in eq. (48). By observing fig. 7, we notice a close resemblance between the SPH simulation results and the analytical solution in eq. (48), thus validating our solver.

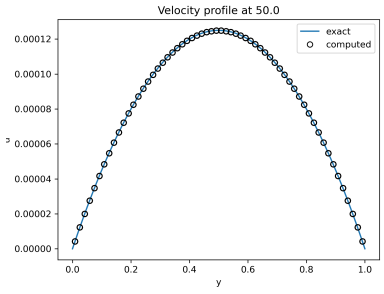

Figure 7: Velocity profile of the Poiseuille flow compared against the analytical solution at time $t = 50$ seconds.

6.2. DEM validation 1: Normal impact of spherical particle

To validate the Discrete Element Method (DEM) solver, we analyze the direct collision between two spherical particles. In fig. 8, the initial setup

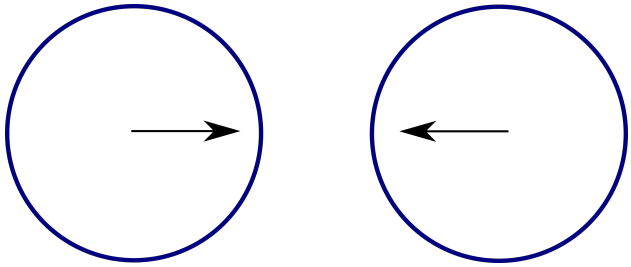

Figure 8: Schematic of two spherical particles of equal radius in a head-on collision with equal magnitude of velocity but opposite direction.

depicts both particles moving towards each other with an initial velocity of 10 $\mathrm{m\,s^{-1}}$. Each ~~disk~~ has a radius of 0.01 m and is composed of glass. The glass material has a Young's modulus of 4.8×10^{10} $\mathrm{N\,m^{-2}}$, a Poisson ratio of 0.2, and a density of 2800 $\mathrm{kg\,m^{-3}}$. For the current scenario, we assume there is no friction among the particles and no gravity acting on the particles. Figure 9 depicts the variation of the normal force and the amount of overlap, compared to the analytical findings presented in [38]. The force curve generated by our current implementation closely matches the analytical result, hereby confirming the validation of our DEM solver's model for normal contact force.

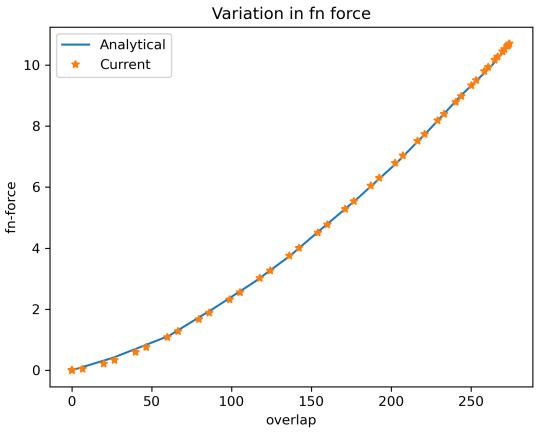

Figure 9: Variation of the normal impact force with overlap of the impacting particles, compared to the analytical result.

6.3. DEM validation 2: Particle wall impact

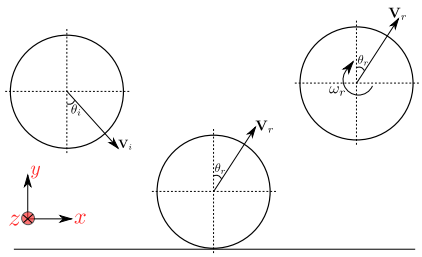

Figure 10: Schematic of a spherical particle impacting a wall with same magnitude of velocity but different impact angles.

As part of our validation test cases, we consider the collision of a spherical particle with wall with different incident angles and a constant velocity in magnitude. This test case is helpful in testing the tangential part of our DEM solver. The schematic of the body and wall is shown in fig. 10. The radius of the impacting particle is 0.0025 m and is made of aluminium oxide. The particle has a Young's modulus of 3.8×10^{11} N m^{-2}, a Poisson ratio of 0.23, and a density of 4000 kg m^{-3}. The wall's Young's modulus is 70×10^{9} N m^{-2}, with a Poisson ratio of 0.25. The impact velocity has a magnitude of 3.9 m s^{-1}. The coefficient of friction between the wall and the particle is 0.092.

In fig. 11, we show variation of the rebound angular velocity with the incident impact angle, compared to experimental data from Kharaz et al. [39]. The angular velocity variation generated by our present implementation closely aligns with the experimental data, thereby validating the tangential component of our DEM solver's contact force model.

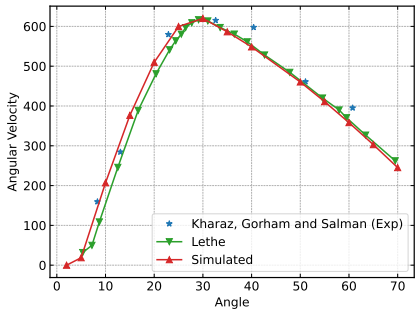

make it larger

Figure 11: Variation of the rebound angular velocity of the impacting particle with the incidence angle, compared to the experimental result and Lethe DEM solver by [37].

6.4. RFC validation 1: Single particle entering into a tank

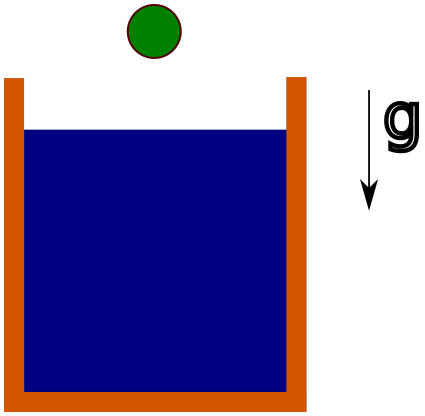

Figure 12: A circular cylinder entering into a calm water tank under the influence of the gravity.

or sphere? or disc ?

To validate the rigid-fluid coupling solver, we examine the motion of a circular cylinder descending into a steady hydrostatic tank, considering two different densities for the cylinder. This scenario has been investigated experimentally by Greenhow and Lin [40] and numerically by various studies, including Sun and Faltinsen [41] using the Boundary Element Method and [42] employing the δ^+-SPH technique. Figure 12 illustrates the initial setup, with the cylinder positioned 0.5 meters from the free surface. The cylinder's radius is 0.11 meters, and we investigate cases with densities of 500 and 1000 kg,m^{-3}. The cylinder descends due to gravity into the tank. We perform tests using three different spacings to assess convergence: resolving the cylinder

diameter into 20, 50, and 80 particles, resulting in spacings of 0.0055 m, 0.0022 m, and 0.001375 m respectively. We employ a kinematic viscosity of 1×10^{-6} m^2/s for water and do not utilize artificial viscosity in this case. The simulation runs for a total time of 0.16 seconds, utilizing a smoothing length (h) equal to the particle spacing in each scenario. The speed of sound is set to ten times the maximum fluid velocity attainable.

Figure 13, depicts the evolution of the depth of penetration of the cylinder, compared against the experimental result by Greenhow and Lin [40], numerical techniques of boundary element method (BEM)([41]) and delta-plus SPH ([42]). From fig. 13, we find that the current solver matches well with the experimental result as well as the numerical studies and also converges while increasing the resolution.

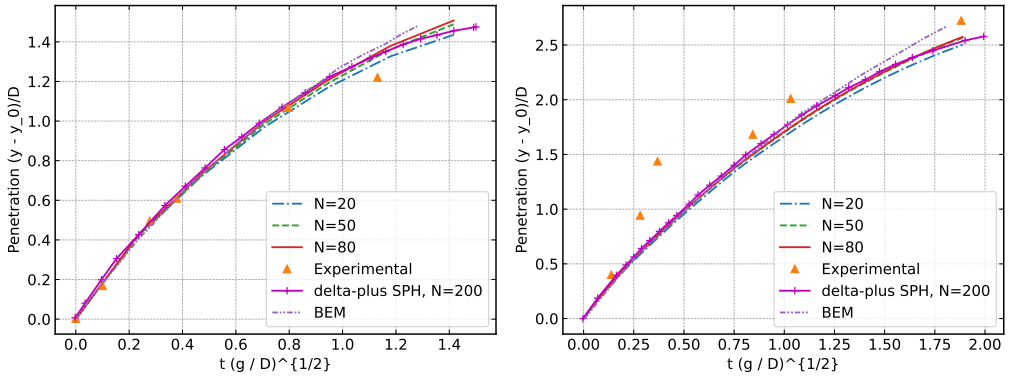

(a) Half buoyant cylinder

(b) Neutrally buoyant cylinder

Figure 13: Variation of the penetration depth of the cylinder with time, compared to BEM model [41] and δ+SPH model[42].

6.5. RFC validation 2: Falling solid in water

The current test case involves falling of a solid cube in a calm water tank. The position of the cube is compared with the experimental[43] result for the validation of the current SPH-DEM solver. This problem has been used as a standard benchmark in validating several other numberical techniques, such as in VOF-DEM solver of [44] and other SPH-DEM solvers [45]. The cube has a side length of 20 mm. While the dimentions of the water tank is 150 mm × 140 mm × 140 mm. While the water depth is taken as 131 mm. The density of the water is taken as 1000 kg,m^{-3}, and the density of the cube is 2120 kg,m^{-3}. The schemtic of the initial configuration is shown in fig. 14.

The tank and the fluid has 150 mm x-direction, out of the plane which is not shown in the schematic. We show that the current solver can handle 3D problems with this test case.

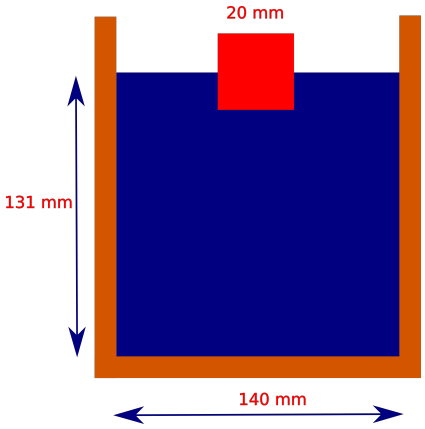

Figure 14: Schematic of a cube of density $2120 kg, m^{-3}$ immersed half way in a steady hydrostatic tank is allowed to settle under gravity.

Figure 15 shows the evolution of the y-position of center of mass of the cube, compared against the experimental result by Wu et al. [43]. From fig. 15, the comparison reveals a close correspondence between the results obtained by our solver and the experimental findings, affirming its capability to handle fluid-solid coupling problems efficiently.

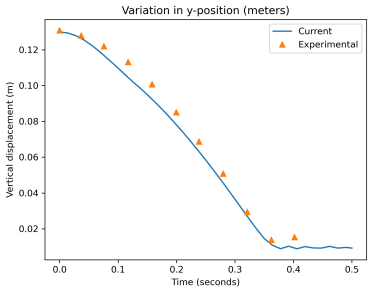

Figure 15: Vertical position variation of the center of mass of the cube with time, compared against the experimental result by Wu et al. [43].

References

1. Wang, X., Gong, L., Li, Y., Yao, J.. Developments and applications of the cfd-dem method in particle–fluid numerical simulation in petroleum engineering: A review. *Applied Thermal Engineering* 2023;222:119865.

2. Dai, Y., Zhang, Y., Li, X.. Numerical and experimental investigations on pipeline internal solid-liquid mixed fluid for deep ocean mining. *Ocean Engineering* 2021;220:108411. URL: https://doi.org/10.1016/j.oceaneng.2020.108411. doi:10.1016/j.oceaneng.2020.108411.

3. Qingyun, Z., Mingxin, Z., Dan, H.. Numerical simulation of impact and entrainment behaviors of debris flow by using SPH–DEM–FEM coupling method. *Open Geosciences* 2022;14(1):1020–1047. URL: https://doi.org/10.1515/geo-2022-0407. doi:10.1515/geo-2022-0407.

4. Karunasena, H., Senadeera, W., Gu, Y., Brown, R.. A coupled SPH-DEM model for micro-scale structural deformations of plant cells during drying. *Applied Mathematical Modelling* 2014;38(15-16):3781–3801. URL: https://doi.org/10.1016/j.apm.2013.12.004. doi:10.1016/j.apm.2013.12.004.

5. Mintu, S., Molyneux, D.. Simulation of ice-structure interactions using a coupled SPH-DEM method. In: *Day 1 Mon, November 05, 2018*. OTC; 2018:URL: https://doi.org/10.4043/29139-ms. doi:10.4043/29139-ms.

6. Li, B., Kang, Q., Wang, Z., Wang, J.. Study of free-surface and solids suspension in top-sealed tanks stirred by pitched blade turbine impellers through dem-vof method. *Asia-Pacific Journal of Chemical Engineering* 2022;17(3):e2758.

7. Xiong, Q., Madadi-Kandjani, E., Lorenzini, G.. A lbm–dem solver for fast discrete particle simulation of particle–fluid flows. *Continuum Mechanics and Thermodynamics* 2014;26:907–917.

8. Kloss, C., Goniva, C., Hager, A., Amberger, S., Pirker, S.. Models, algorithms and validation for opensource dem and cfd–dem. *Progress in Computational Fluid Dynamics, an International Journal* 2012;12(2-3):140–152.

9. Peng, C., Zhan, L., Wu, W., Zhang, B.. A fully resolved sph-dem method for heterogeneous suspensions with arbitrary particle shape. *Powder Technology* 2021;387:509–526.

10. Li, J.J., Qiu, L.C., Tian, L., Yang, Y.S., Han, Y.. Modeling 3d non-newtonian solid–liquid flows with a free-surface using dem-mps. *Engineering Analysis with Boundary Elements* 2019;105:70–77.

11. Franci, A., de Pouplana, I., Casas, G., Celigueta, M.Á., González-Usúa, J., Oñate, E.. Pfem–dem for particle-laden flows with free surface. *Computational Particle Mechanics* 2020;7:101–120.

12. Cleary, P.W.. Prediction of coupled particle and fluid flows using dem and sph. *Minerals Engineering* 2015;73:85–99.

13. Trujillo-Vela, M.G., Galindo-Torres, S.A., Zhang, X., Ramos-Cañón, A.M., Escobar-Vargas, J.A.. Smooth particle hydrodynamics and discrete element method coupling scheme for the simulation of debris flows. *Computers and Geotechnics* 2020;125:103669.

14. van der Hoef, M.A., van Sint Annaland, M., Deen, N., Kuipers, J.. Numerical simulation of dense gas-solid fluidized beds: a multiscale modeling strategy. *Annu Rev Fluid Mech* 2008;40:47–70.

15. Ma, H., Zhou, L., Liu, Z., Chen, M., Xia, X., Zhao, Y.. A review of recent development for the cfd-dem investigations of non-spherical particles. *Powder Technology* 2022;412:117972.

16. Brosh, T., Kalman, H., Levy, A.. Accelerating cfd–dem simulation of processes with wide particle size distributions. *Particuology* 2014;12:113–121.

17. Li, X., Zhao, J.. Dam-break of mixtures consisting of non-newtonian liquids and granular particles. *Powder Technology* 2018;338:493–505.

18. Zhu, H., Zhou, Z., Yang, R., Yu, A.. Discrete particle simulation of particulate systems: a review of major applications and findings. *Chemical Engineering Science* 2008;63(23):5728–5770.

19. Gingold, R.A., Monaghan, J.J.. Smoothed particle hydrodynamics: theory and application to non-spherical stars. *Monthly notices of the royal astronomical society* 1977;181(3):375–389. doi:10.1093/mnras/181.3.375.

20. Lucy, L.B.. A numerical approach to the testing of the fission hypothesis. *The astronomical journal* 1977;82:1013–1024. doi:10.1086/112164.

21. Monaghan, J.J.. Smoothed particle hydrodynamics and its diverse applications. *Annual Review of Fluid Mechanics* 2012;44:323–346.

22. Markauskas, D., Kruggel-Emden, H.. Coupled dem-sph simulations of wet continuous screening. *Advanced Powder Technology* 2019;30(12):2997–3009.

23. Canelas, R.B., Crespo, A.J., Domínguez, J.M., Ferreira, R.M., Gómez-Gesteira, M.. Sph–dcdem model for arbitrary geometries in free surface solid–fluid flows. *Computer Physics Communications* 2016;202:131–140.

24. Amicarelli, A., Albano, R., Mirauda, D., Agate, G., Sole, A., Guandalini, R.. A smoothed particle hydrodynamics model for 3d solid body transport in free surface flows. *Computers & fluids* 2015;116:205–228.

25. Asai, M., Li, Y., Chandra, B., Takase, S.. Fluid–rigid-body interaction simulations and validations using a coupled stabilized isph–dem incorporated with the energy-tracking impulse method for multiple-body contacts. *Computer Methods in Applied Mechanics and Engineering* 2021;377:113681.

26. Monaghan, J.J., Kajtar, J.B.. Sph particle boundary forces for arbitrary boundaries. *Computer physics communications* 2009;180(10):1811–1820.

27. Park, H.J., Seo, H.D.. A new sph-fem coupling method for fluid–structure interaction using segment-based interface treatment. *Engineering with Computers* 2023;:1–17.

28. Zou, L., Sun, J.Z., Sun, Z., Yu, Z.B., Zhao, H.B.. Study of two free-falling spheres interaction by coupled sph–dem method. *European Journal of Mechanics-B/Fluids* 2022;92:49–64.

29. Ng, K., Alexiadis, A., Chen, H., Sheu, T.. Numerical computation of fluid–solid mixture flow using the sph–vcpm–dem method. *Journal of Fluids and Structures* 2021;106:103369.

30. Ramachandran, P., Bhosale, A., Puri, K., Negi, P., Muta, A., Dinesh, A., Menon, D., Govind, R., Sanka, S., Sebastian, A.S., et al. Pysph: a python-based framework for smoothed particle hydrodynamics. *ACM Transactions on Mathematical Software (TOMS)* 2021;47(4):1–38.

31. Ramachandran, P.. automan: A python-based automation framework for numerical computing. *Computing in Science & Engineering* 2018;20(5):81–97.

32. Violeau, D., Rogers, B.D.. Smoothed particle hydrodynamics (SPH) for free-surface flows: past, present and future. *Journal of Hydraulic Research* 2016;54:1–26.

33. Morris, J.P., Fox, P.J., Zhu, Y.. Modeling low reynolds number incompressible flows using sph. *Journal of computational physics* 1997;136(1):214–226.

34. Monaghan, J.J.. Smoothed Particle Hydrodynamics. *Reports on Progress in Physics* 2005;68:1703–1759.

35. Adami, S., Hu, X., Adams, N.. A generalized wall boundary condition for smoothed particle hydrodynamics. *Journal of Computational Physics* 2012;231(21):7057–7075. doi:10.1016/j.jcp.2012.05.005.

36. Brilliantov, N.V., Spahn, F., Hertzsch, J.M., Pöschel, T.. Model for collisions in granular gases. *Physical review E* 1996;53(5):5382.

37. Golshan, S., Munch, P., Gassmöller, R., Kronbichler, M., Blais, B.. Lethe-dem: An open-source parallel discrete element solver with load balancing. *Computational Particle Mechanics* 2023;10(1):77–96.

38. Chung, Y., Ooi, J.. Benchmark tests for verifying discrete element modelling codes at particle impact level. *Granular Matter* 2011;13(5):643–656.

39. Kharaz, A., Gorham, D., Salman, A.. An experimental study of the elastic rebound of spheres. *Powder Technology* 2001;120(3):281–291.

40. Greenhow, M., Lin, W.M.. Nonlinear free surface effects: experiments and theory. Massachusetts Institute of Technology, Department of Ocean Engineering Cambridge; 1983.

41. Sun, H., Faltinsen, O.M.. Water impact of horizontal circular cylinders and cylindrical shells. *Applied Ocean Research* 2006;28(5):299–311.

42. Sun, P., Zhang, A.M., Marrone, S., Ming, F.. An accurate and efficient sph modeling of the water entry of circular cylinders. *Applied Ocean Research* 2018;72:60–75.

43. Wu, T.R., Chu, C.R., Huang, C.J., Wang, C.Y., Chien, S.Y., Chen, M.Z.. A two-way coupled simulation of moving solids in free-surface flows. *Computers & Fluids* 2014;100:347–355.

44. Nan, X., Hou, J., Shen, Z., Tong, Y., Li, G., Wang, X., Kang, Y.. Cfd-dem coupling with multi-sphere particles and application in predicting dynamic behaviors of drifting boats. *Ocean Engineering* 2022;247:110368.

45. Qiu, L.C., Liu, Y., Han, Y., et al. A 3d simulation of a moving solid in viscous free-surface flows by coupling sph and dem. *Mathematical Problems in Engineering* 2017;2017.